Creating Nanoparticle Stability in Ionic Liquid $[C_4mim][BF_4]$ by Inducing Solvation Layering

Jingsi Gao,[†] Rose S. Ndong,[†,§] Mark B. Shiflett,[‡] and Norman J. Wagner*[,†]

[†]Center for Molecular and Engineering Thermodynamics, Department of Chemical and Biomolecular Engineering, University of Delaware, Newark, Delaware 19716, United States and [‡]Central Research and Development, DuPont Company, Wilmington, Delaware 19880, United States. [§]Present address: Solvay USA Inc., 350 George Patterson Boulevard, Bristol, Pennsylvania 19007, United States.

ABSTRACT The critical role of solvation forces in dispersing and stabilizing nanoparticles and colloids in 1-butyl-3-methylimidazolium tetrafluoroborate $[C_4mim][BF_4]$ is demonstrated. Stable silica nanoparticle suspensions over 60 wt % solids are achieved by particle surface chemical functionalization with a fluorinated alcohol. A combination of techniques including rheology, dynamic light scattering (DLS), transmission electron microscopy (TEM), and small angle neutron scattering (SANS) are employed to determine the mechanism of colloidal stability. Solvation layers of ~5 nm at room temperature are measured by multiple techniques and are thought to be initiated by hydrogen bonds between the anion $[BF_4]^-$ and the fluorinated group on the surface coating. Inducing structured solvation layering at particle surfaces through hydrogen bonding is demonstrated as a method to stabilize particles in ionic liquids.

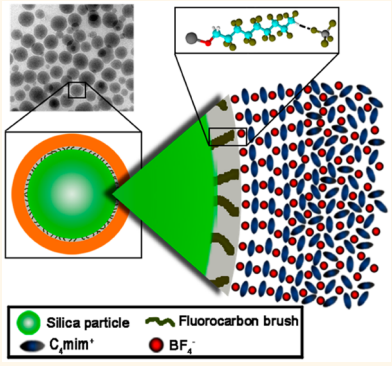

KEYWORDS: ionic liquids · nanoparticles · solvation layers · dispersion stability · rheology

Room temperature ionic liquids have received considerable interest in various fields including separations,[1] catalysis,[1−4] electrolytes,[5,6] heat transfer,[7,8] and drug delivery.[9] Their unique physicochemical properties suggest they can be used as a "green" replacement for traditional organic solvents,[1−3] as lubricants for space and high vacuum environments,[10−12] as separation media for batteries, fuel cells,[4] dye sensitized solar cells,[5] and more recently, for industrial scale carbon capture from flue gases.[13] The wide variety of available cations and anions provide a high flexibility in material design, but a thermodynamic database necessary to develop structure−property relationships is still under development.[14]

Many applications of ionic liquids require successfully dispersing nanoparticles across a broad range of conditions. Studies of colloidal systems in ionic liquids include nanoparticle synthesis,[15,16] phase transfer,[17] catalytic reactions medium as a "green" solvent,[1−3,18] the self-assembly of surfactants,[19,20] and block copolymer mesophases.[21,22] However, there are relatively few studies of the stability of colloidal particles in ionic liquids and these have been primary empirical,[23−30] despite the fact that nanoparticle stability is of critical importance in determining the suspension rheology and controlling aggregation, gel and glass formation, as well as in the performance of ionic liquid based lubricants. It is apparent from the limited reports in the literature that particle dispersion and stability in ionic liquids depends on the specific chemical composition of the ionic liquid as well as the surface chemistry of the particles.[24,29,30]

The shear viscosity of hydrophilic and hydrophobic fumed silica colloidal dispersions in various ionic liquids were measured, in which shear thinning, shear thickening, and gelation were reported.[24] An increase of the alkyl chain length of the cation has been reported as beneficial for stabilizing TiO_2 nanopowders in 1-alkyl-3-methylimidazolium tetrafluoroborate ($[C_nmim][BF_4]$) ionic liquids.[29] Spherical silica nanoparticles were reported to aggregate in imidazolium-based ionic liquids by Ueno *et al.*,[27] while

* Address correspondence to wagnernj@udel.edu.

Received for review January 16, 2015 and accepted March 10, 2015.

Published online March 10, 2015
10.1021/acsnano.5b00354

© 2015 American Chemical Society

grafting polymer such as poly(methyl methacrylate) (PMMA) to the particle surface improved suspension stability in ionic liquids.[23,27] For example, PMMA-grafted silica nanoparticles show good dispersion in 1-butyl-3-methylimidazolium hexafluorophosphate ($[C_4mim][PF_6]$) and 1-alkyl-3-methylimidazolium bis-(trifluoromethylsulfonyl)imide ($[C_nmim][NTf_2]$), presumably because PMMA is itself soluble in these solvents; however, such coated particles show poor dispersion if PMMA is insoluble in the ionic liquids (*e.g.*, $[C_4mim][BF_4]$).[27] Here the mechanism of stability is afforded by the steric repulsion between the grafted layers of significant extent and as is typical with such systems, the system will become unstable when the brush is immersed into a poor solvent and collapses.[31]

Particle stability in dispersions is typically treated within the classical framework of colloid science, namely the Derjaguin–Landau–Verwey–Overbeek (DLVO) theory, which accounts for van der Waals attraction and electrostatic repulsion between particles in solution.[32] Because of the ionic nature of the solvent, electrostatic stabilization is not sufficient to stabilize particles in ionic liquids against the ubiquitous attraction from dispersion forces between the particles.[27] The high ionic strength in ionic liquids effectively screens the electrostatic repulsion between silica particles. The screening of the electrical potential and electrical double layers at charged solid surfaces in ionic liquids and molten salts[33] has been investigated by experiments[34] and simulations.[35,36] The electrical double layer in ionic liquid $[C_4mim][BF_4]$ has been determined to be one-ion thick layer (about 0.4 nm thickness) using sum frequency generation vibrational spectroscopy (SFG), electrochemical impedance spectroscopy (EIS), and the vibrational Stark effect.[34]

Because of this screening, surface-adsorbed or grafted surfactants and polymers soluble in the ionic liquid are introduced to provide stability.[31] However, there are rare cases where "bare" particles disperse into ionic liquids; *e.g.*, hydrophilic fumed silica particles can be dispersed into an aprotic ionic liquid, $[C_4mim][BF_4]$ in the absence of any stabilizer.[24,26,37] This unexpected stability is hypothesized to be induced by solvation forces arising from solvent structuring near the particle surfaces, and the fact that the particles are often porous aggregates such that van der Waals attractions are weak.[23,26,37] There is evidence for such solvation forces occurring at macroscopic surfaces: Oscillating solvation forces have been observed between macroscopic mica and silica surfaces in both protic and aprotic ionic liquids as detected by surface force measurements,[38–43] and these observations have been qualitatively reproduced by molecular dynamics simulation.[44] These measurements and simulations indicate that the ion pairs are arranged in a layered structure near the solid surfaces.[42] Other evidence supporting the existence of solvation layers in particle

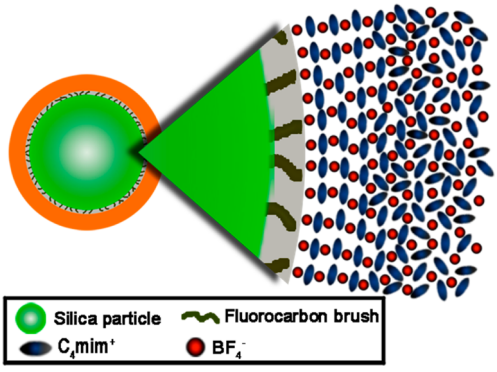

Figure 1. Schematic illustration of a coated silica nanoparticle stabilized by solvation layers in ionic liquid $[C_4mim][BF_4]$. Note the ion structure in the layers is schematic.

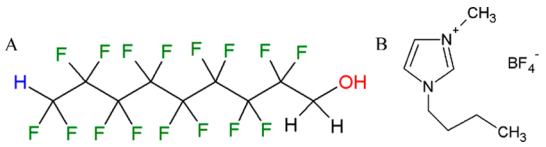

Figure 2. Chemical structure of fluorocarbon 1*H*,1*H*,9*H*-hexadecafluoro-1-nonanol used to functionalize the particle surface (A) and ionic liquid 1-butyl-3-methylimidazolium tetrafluoroborate ($[C_4mim][BF_4]$) (B).

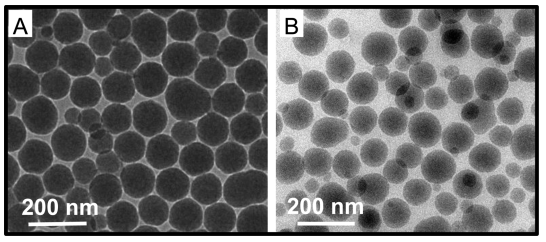

Figure 3. Transmission electron microscopy (TEM) images of (A) the dried fluorocarbon-coated particle and (B) fluorocarbon-coated particles in $[C_4mim][BF_4]$.

dispersions include the increase in fumed silica particle stability in $[C_4mim][BF_4]$ upon addition of lithium salt which is presumed to stabilize the solvation layers.[37] Furthermore, silica particle suspensions lose stability in the presence of small amounts of water, which decreases the structuring of solvation layers.[26,45] However, to date, there are no direct measurements of the solvation-induced structuring in ionic liquids around nanoparticle surfaces or a predictive, quantitative knowledge of interparticle interactions in ionic liquids that can be used to predict and control colloidal stability.

To directly test this hypothesis and to develop a strategy for dispersing nanoparticles in ionic liquids more generally, we study the nanostructure, stability, and dynamics of model, spherical silica particles (NexSil 125–40, Nyacol Nano Technologies, Inc.), surface-functionalized in a common aprotic ionic liquid $[C_4mim][BF_4]$. Surface modification using a small fluorocarbon molecule, 1*H*,1*H*,9*H*-hexadecafluoro-1-nonanol (CAS #376–18–1), induces solvation layering around

TABLE 1. Summary of Particle Radii for Uncoated and Coated Particles with Various Methods

Measurement Techniques	Uncoated particle in H_2O	Coated particle in ethanol	Coated particle in $[C_4mim][BF_4]$
DLS	53.8 ± 4.8 nm	55.2 ± 3.8 nm	60.4 ± 3.0 nm
SANS	54.2 ± 5.4 nm	Core: 54.2 ± 5.4 nm	Core: 54.2 ± 5.4 nm
	p = 10.5 %	p = 10.5 %	p = 10.5 %
Brush	…	0.9 nm	1.2 nm
Schematic illustration			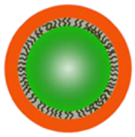

silica particles, leading to dispersion stability. The choice of this surface modifier is motivated by the research of Shiflett and Yokozeki,[46] who studied the behavior of fluorocarbons in room temperature ionic liquids and found a wide range of solubility that correlated with hydrogen bonding. We propose that hydrogen bonding between the fluorinated anion in the ionic liquid $[C_4mim][BF_4]$ (Figure 2B) and the terminal hydrogen group on the surface coating (Figure 2A) drives the formation of solvation layers that impart colloidal stability by steric repulsion. Figure 1 shows a schematic representation of such solvation layers, based on the dimensions determined in this work. Note that our methods cannot determine the molecular orientation in the layers and the molecular details in the schematic are based on related literature work.[42,43] This study presents the first direct measurements of the extent of the formation of these solvation layers around nanoparticles in ionic liquid $[C_4mim][BF_4]$ using transmission electron microscopy (TEM), rheology, dynamic light scattering (DLS), and small angle neutron scattering (SANS).

RESULTS AND DISCUSSION

The silica nanoparticles as supplied are dispersed in water, but aggregate if dispersed into $[C_4mim][BF_4]$. This is in direct contrast to the surface functionalized nanoparticles: fluorocarbon-coated nanoparticles readily disperse and remain stable in $[C_4mim][BF_4]$, but do not disperse in water. Transmission electron microscopy (TEM) images comparing the dried fluorocarbon-coated silica particles and fluorocarbon-coated silica nanoparticles dispersed in $[C_4mim][BF_4]$ are shown in Figure 3. The synthesis procedure for coating the fluorocarbon to the surface of the silica nanoparticle has no effect on the silica nanoparticle core shape or size. Figure 3B shows the dispersion of the particles by direct observation using *in situ* TEM, which is possible in the ionic liquid medium despite the high vacuum condition and electron beam irradiation of electron microscope chamber.[16] The lower resolution for the image in the ionic liquid is due in part to the Brownian motion of the particles and possible flow of the dispersion on the grid during the imaging.

The hydrodynamic radii of uncoated and coated silica nanoparticles in polar solvents and the ionic liquid are measured by dynamic light scattering (see Supporting Information). The results in ethanol demonstrate that addition of the fluorocarbon coating increases the radius of particles (Table 1) by an amount consistent with the molecular size of the fluorocarbon (∼1.4 nm) as calculated from the bond lengths and angles. However, there is an anomalous increase in hydrodynamic radius observed for the particles dispersed in the ionic liquid. Detailed analysis of the size distributions (Supporting Information), coupled with the direct TEM observations, show that this increase in hydrodynamic size is not due to a small amount of aggregation, but rather, is the consequence of solvation layers forming near the particle surface that increase the hydrodynamic size of the particles. Note that the uncoated silica particles will not disperse in $[C_4mim][BF_4]$ even after sonication and extensive mixing; DLS measurements on these systems yield a broader size distribution and a much larger particle size indicative of aggregation.

The interaction potentials between two silica particles in solution can be calculated from the DLVO theory. The parameters used to calculate the van der Waals, electrostatic, and DLVO potentials are listed in Table 2. The DLVO potential profiles of two uncoated silica nanoparticles (R = 54.2 nm) in $[C_4mim][BF_4]$ and mother liquid at 25 °C are shown in Figure 4 as a function of the surface separation distance d. The DLVO potential for silica nanoparticles in the aqueous mother liquid is positive for d > 0.1 nm (Figure 4B), indicating long-range repulsion leading to particle stabilized by electrostatic forces, in agreement with

observation. However, for silica nanoparticles dispersed in $[C_4mim][BF_4]$ as shown in Figure 4A, the electrostatic repulsion is screened and the DLVO potential is negative, indicating the particles are attracted to each other at all separation distances. Thus, the DLVO calculations predict that the uncoated silica particles can be electrostatically stabilized in mother liquid, but not in $[C_4mim][BF_4]$, which agrees with experimental results.

The addition of the fluorocarbon coating will provide a steric barrier to keep particles apart. However, the calculations in Figure 4A show that the particles with the fluorocarbon will still have a weak attraction $O(k_BT)$ sufficient to induce weak flocculation if the coating acts as a ~1 nm steric layer keeping particle surfaces ~2 nm apart. However, DLS measurements show that the silica nanoparticles are surrounded by ~5 nm solvation layers such that minimum separations of $d \approx 10$ nm are anticipated. At this separation distance, the DLVO attractive potential between nanoparticles is negligible (Figure 4A), confirming that these coated nanoparticles can be stabilized by inducing the formation of solvation layers in $[C_4mim][BF_4]$.

Small angle neutron scattering (SANS) measurements of dilute nanoparticle suspensions are performed to further quantify the particle size, polydispersity, and coating layer structure. Furthermore, SANS measurements of a concentration series enable detecting the particle stabilization mechanism through direct measurement of the structure factor.

The measured SANS scattering intensities for dilute dispersions ($\phi = 0.004$) of uncoated and coated particles in different solvents at 25 °C are shown in Figure 5.

TABLE 2. Parameters for the Calculation of the DLVO Potential for Colloidal Dispersions in $[C_4mim][BF_4]$ and H_2O/Mother Liquid at 25 °C

materials	ε	n	A (10^{-21} J)	ψ_s (mV)	M (mol/L)	κ^{-1} (nm)
silica	4.42	1.46	—	—	—	—
$[C_4mim][BF_4]$	11.70	1.42	1.04	−9.48	—	0.4
H_2O/mother liquid	78.54	1.33	6.97	−36.57	1×10^{-4}	30.5

The general shapes of the scattering spectra are similar as expected, given that the particles have the same core, which dominates the scattering intensity. The differences in scattering intensities reflect differences in the neutron scattering length densities of the solvents, which is also evident in the different background intensities observed at high values of scattering vector q. The scattering intensity from the dispersion of uncoated particles in H_2O is fitted by varying particle size, polydispersity, and volume fraction with a Schulz-distributed sphere model[47] using the known scattering length densities (SLD) for the core and solvent. The measured scattering intensities from dispersions of coated particles in ethanol and $[C_4mim][BF_4]$ are fitted by a core−shell model and varying the shell thickness, volume fraction, and scattering length density of the shell under constraints. The fitting parameters are summarized in Table 3. In the fitting, the volume fraction of the dispersion is restricted with the particle concentration calculated from mass with uncertainty, the shell thickness is constrained by the extended molecular size of fluorocarbon, and the scattering length density of the shell is constrained within the range of the SLD of solvent and fluorocarbon. From the fits, we extract individual particle properties such as core size, polydispersity, and coating thickness. As the density of ionic liquid solvation layers is close to the bulk ionic liquid, there is no significant scattering length density difference between solvation layers

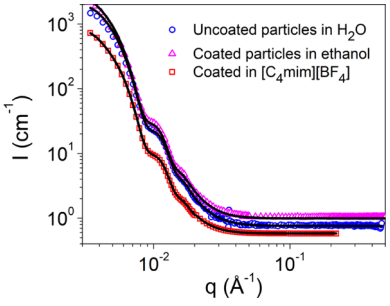

Figure 5. Measured SANS scattering intensity at 25 °C for three dilute dispersions and corresponding fits: uncoated particles in H_2O, coated particles in ethanol and in ionic liquid $[C_4mim][BF_4]$, respectively.

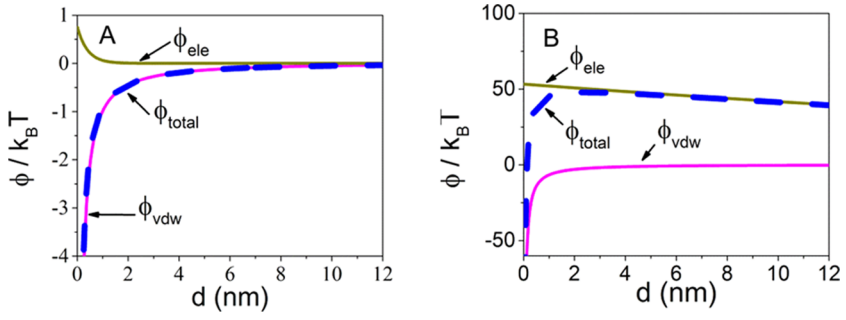

Figure 4. Calculated DLVO interparticle potential profiles at $T = 25$ °C for silica particles in $[C_4mim][BF_4]$ (A) and in 0.1 mM (pH = 9.1 ± 0.1) NaCl aqueous solution (mother liquid) (B).

TABLE 3. Parameters Used for SANS Form Factor Fittings

parameters	uncoated particles in H_2O	coated particles in ethanol	coated particles in $[C_4mim][BF_4]$
ϕ	0.0036[b]	0.0048[b]	0.0032[b]
$\bar{r}$ (nm)	54.2[b]	54.2[a]	54.2[a]
p	0.105[b]	0.105[a]	0.105[a]
δ (shell, nm)	—	0.9[b]	1.2[b]
SLD_{core} (A^{-2})	3.47×10^{-6}[a]	3.47×10^{-6}[a]	3.47×10^{-6}[a]
SLD_{shell} (A^{-2})	—	3.24×10^{-6}[b]	3.24×10^{-6}[b]
$SLD_{solvent}$ (A^{-2})	-5.60×10^{-6}[a]	-3.45×10^{-7}[a]	1.40×10^{-6}[a]
background (cm^{-1})	0.76[a]	0.99[a]	0.62[a]

[a] The parameters are fixed as constant. [b] The parameters are fitted under constraints.

and the ionic liquid. Therefore, the solvation layers are not detected directly by neutron scattering. We note that the shell SLD determined from the fit is close to the value calculated for the pure fluorocarbon. This suggests that the large molecular size of fluorine of the fluorocarbon chains (fluorocarbon chains occupy 60 vol % of the shell) prevents significant solvent penetration into the coating. Analysis of the SANS form factor measurements, summarized in Table 1, yield a particle radius of 54.2 ± 5.4 nm for the core particles with 10.5% polydispersity (p) and shell thickness of 0.9 and 1.2 nm for particles dispersed in ethanol and $[C_4mim][BF_4]$, respectively. These measurements further confirm the presence of the fluorocarbon coating and show that the fluorocarbon brush is more extended in $[C_4mim][BF_4]$, which suggests better compatibility with $[C_4mim][BF_4]$ than with ethanol.

The average radii of the uncoated and coated particles obtained from DLS and SANS are summarized and compared in Table 1. An estimate of the solvation layer of ~5 nm can be made by comparing the difference between the hydrodynamic radius in $[C_4mim][BF_4]$ measured by DLS and the core−shell radius determined by SANS measurements. A solvation layer is not detected by SANS fits to the form factor, but will increase the particle radius and thus, slow diffusion and yield an apparently larger particle in DLS.

SANS measurements on more concentrated dispersions of the coated particles in $[C_4mim][BF_4]$ are reported in Figure 6, with scattering intensity $I(q)$ *versus* scattering wave vector q systematically shifted vertically for clarity. With increasing particle concentration, a structure peak becomes evident for $q < 0.01$ Å^{-1}. The scattering intensities are analyzed by fitting to eq 10 (defined in Methods section) with an effective structure factor. From these fits, we determine the potential parameters that include an effective particle size and strength of attraction. In the analysis, the particle form factor is accurately represented by a polydisperse core−shell form factor model[47] with all of the associated parameters measured from the dilute sample shown in Figure 5.

The solvation layers detected by DLS should also be evident in the structure factor as they provide steric

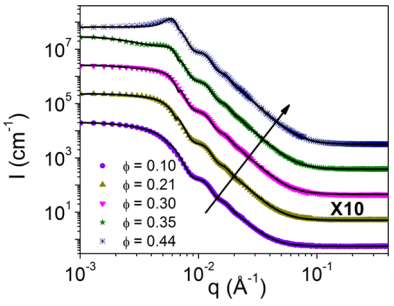

Figure 6. SANS intensity I *versus* scattering wave vector q as a function of particle concentration for 25 °C and the corresponding sticky-hard sphere model fits. (The scattering intensities are systematically shifted by a factor of 10 for clarity.)

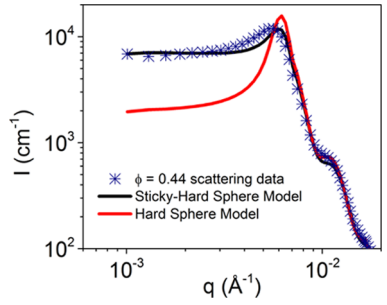

Figure 7. SANS intensity of ϕ = 0.44 coated particle $[C_4mim][BF_4]$ dispersion with sticky-hard sphere and hard sphere model fits.

stability and thus, prevent particles from approaching closely. Consequently, solvation layers will lead to a dispersion structure reflecting this increased, larger particle size. Examination of Figure 7 shows that an effective hard sphere potential with an effective radius that includes the solvation layer can capture the location of the intensity peak, but is still not sufficient to describe the suspension microstructure as there are still weak interparticle attractions. To improve the description we use the simplest model that includes both excluded volume and attractions—the "sticky" effective hard sphere model—and calculate the structure factor $S(q)$ accordingly.[47] This structure factor depends on the effective volume fraction (defined in eq 10 in Methods section) in a self-consistent manner

TABLE 4. Summary of Structure Factor Fitting Parameters for Dispersions Coated Nanoparticles in $[C_4mim][BF_4]$ Corresponding to Figure 6,[a]

parameters	$\phi = 0.100$	$\phi = 0.207$	$\phi = 0.295$	$\phi = 0.352$	$\phi = 0.436$
weight percent	17%	32%	44%	50%	61%
ϕ_{eff}	0.106	0.225	0.340	0.441	0.545
$\bar{r}$ (nm)	54.2	54.2	54.2	54.2	54.2
p	0.105	0.105	0.105	0.105	0.105
δ (shell, nm)	1.2	1.2	1.2	1.2	1.2
SLD_{core} (A^{-2})	3.47×10^{-6}	3.47×10^{-6}	3.47×10^{-6}	3.47×10^{-6}	3.47×10^{-6}
SLD_{shell} (A^{-2})	3.24×10^{-6}	3.24×10^{-6}	3.24×10^{-6}	3.24×10^{-6}	3.24×10^{-6}
$SLD_{solvent}$ (A^{-2})	1.40×10^{-6}	1.40×10^{-6}	1.40×10^{-6}	1.40×10^{-6}	1.40×10^{-6}
perturbation ε	0.01	0.01	0.01	0.01	0.01
Baxter parameter τ	0.70	0.59	0.32	0.16	0.46
background (cm^{-1})	0.56	0.50	0.45	0.39	0.32
$\bar{r}_{eff}$ (nm)	56.3	56.9	58.1	59.7	59.7
Δr_{solv} (nm)	0.9	1.5	2.7	4.3	4.3

[a] The effective volume fraction ϕ_{eff} and stickiness parameter τ are set to float during fitting and the other parameters are set to be fixed value. The average effective particle radii $\bar{r}_{eff}$ and solvation layer thickness Δr_{solv} are calculated from effective volume fraction.

as the number of particles and their effective volume is known in terms of the effective radius. The particles' effective volume fraction can be extracted from the structure factor modeling, keeping the form factor parameters fixed. The sticky hard sphere structure factor fitting parameters and the resultant thicknesses of the solvation layer at each volume fraction are shown in Table 4. The solvation layers thickness determined in this manner is slightly less than, but comparable to, the value of 5 nm ascertained from the DLS measurements. Note that the accuracy of the analysis improves with increasing particle concentration as the structure becomes more prominent. Attempts to fit the data with various potential models without including the solvation shell were unsuccessful. The increase in effective solvation layer thickness with increasing particle concentration trend is expected in part as close approach of surfaces creates confinement, which can induce more ordering in ionic liquids. It is reported in literature that the solvation layers between confined flat surfaces become more ordered as the surface separation decreases, resulting in thicker solvation layer.[39]

The rheological properties of dispersions depend strongly on nanoparticle stability and interparticle interactions, such as solvation layers.[31] Rheological measurements were performed to further explore the effect of the solvation layer formation in the ionic liquid. A suspension of coated nanoparticles dispersed in $[C_4mim][BF_4]$ at moderate concentrations ($\phi = 0.2$) displays near Newtonian behavior, as shown in Figure 8. This further confirms their excellent dispersion due to the effect of the coating. The corresponding zero shear and high shear relative viscosity are $\eta_{r,0} = 2.65 \pm 0.05$ and $\eta_{r,\infty} = 2.51 \pm 0.03$, respectively. These viscosities are larger than expected for a hard sphere dispersion based on the silica volume fraction,[48,49] as shown in Figure 8. Mode coupling theory with $\phi_g = 0.57$[49] is

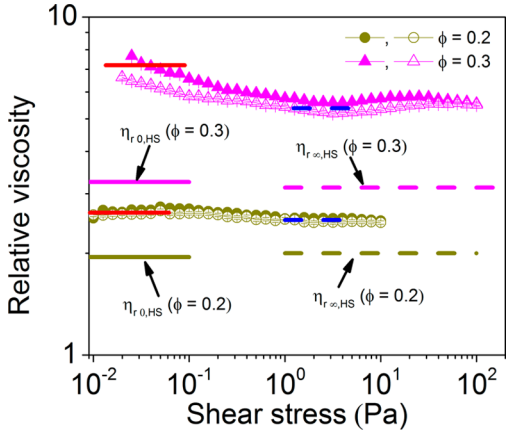

Figure 8. Relative viscosity (with error bar) *versus* shear stress for $\phi = 0.2$ and 0.3 stable suspension of fluorocarbon-coated silica nanoparticles in $[C_4mim][BF_4]$. Closed symbols are ascending stress curves and the open symbols are descending stress curves. The solid lines are the corresponding relative zero shear viscosity; the dashed lines are the corresponding relative high shear viscosity.

employed for hard sphere zero shear relative viscosity; and van der Werff correlation function with $\phi_m = 0.71$[48] is used for hard sphere high shear relative viscosity. The extent of the solvation layer responsible for this increase in viscosity can be deduced from effective particle sizes obtained by fitting the measured zero and high shear viscosities to hard sphere correlations. These values are shown in Table 5 and the corresponding solvation layer thicknesses are calculated to be 5.2 ± 0.2 nm and 4.3 ± 0.3 nm, respectively for the dispersion. The results are in good agreement with the solvation layer thickness determined by DLS and SANS. Further, the reduction in solvation layer thickness at high shear stress is expected as these layers can be displaced by force; however the accuracy of this method is not sufficient to draw further conclusions about this reduction.

TABLE 5. Summary of Relative Viscosity, Effective Volume Fraction and Solvation Layer Thickness Calculated from Shear Flow Curves of ϕ = 0.2 and 0.3 Suspensions

	ϕ = 0.209		ϕ = 0.309	
parameters	zero shear	high shear	zero shear	high shear
η_r (HS)	1.95	2.00	3.25	3.13
η_r (measured)	2.65 ± 0.05	2.51 ± 0.03	7.34 ± 0.49[a]	5.46 ± 0.20
ϕ_{eff}	0.274 ± 0.003	0.262 ± 0.002	0.406 ± 0.006[a]	0.406 ± 0.006
$\bar{r}_{eff}$ (nm)	60.6 ± 0.1	59.7 ± 0.2	60.7 ± 0.1[a]	60.7 ± 0.1
Δr_{solv} (nm)	5.2 ± 0.2	4.3 ± 0.3	5.3 ± 0.2[a]	5.3 ± 0.2

[a] ϕ_{eff} is calculated from high shear relative viscosity of ϕ = 0.309 dispersion and is used to predict the corresponding zero shear relative viscosity η_r (measured).

Interestingly, at higher concentration (ϕ = 0.3), the suspension shows slight shear thickening for shear stresses exceeding 4 Pa. This is to be expected for such dispersions with stabilizing layers that are only slightly permeable to the suspending medium, such as solvation layers.[50,51] Further, the zero shear viscosity is not well-defined and there is some hysteresis in the experiments, both of which are evidence for weak attractive interactions. The same analysis is applied only for the high shear relative viscosity, which is taken as the minimum of the viscosity curve. The thickness of the solvation layer is estimated to be 5.3 ± 0.2 nm. The corresponding zero shear viscosity is predicted using the effective volume fraction obtained from fitting the high shear viscosity as shown in Figure 8, and this value agrees with measured values to within the variation in the data. These solvation layer thicknesses calculated from rheological measurements are in good agreement with the hydrodynamic radius from DLS and those obtained from SANS structure factor measurements. Interestingly, both the SANS and the rheological measurements suggest the presence of weak attractive interactions that are not expected based on the simple DLVO interaction, suggesting that the van der Waals forces are underestimated for this system.

CONCLUSIONS

We have demonstrated a method to spontaneously disperse silica particles in ionic liquid [C_4mim][BF_4] by inducing solvent structuring around the surface of the particle. Extensive characterization of fluorocarbon (1*H*,1*H*,9*H*-hexadecafluoro-1-nonanol) coated silica nanoparticles suspended in ionic liquid [C_4mim][BF_4] by DLS, SANS, TEM and rheology all confirm the presence of a solvation layer of approximately five nanometers. This layer is sufficient to provide steric stabilization against the dispersion attractions. The thickness of this layer is quantitatively similar to that measured for this ionic liquid structuring near flat mica surfaces using surface forces apparatus.[23,42] The five nanometers layer thickness corresponds to seven ion-pair layers, each with 0.7 to 0.8 nm thickness as measured using surface forces.[40] The number of layers is also consistent with the measurements of Perkin *et al.*[42,52] on the structuring of [C_4mim][NTf_2] confined between mica.

In much of the analyses presented here it is assumed for simplicity that the solvation layers form a well-defined, uniform shell surrounding the nanoparticles. However, the solvation layers near flat substrates are expected to become less organized and smoothly transition to the bulk liquid, as shown by surface force apparatus (SFA),[42,43] atomic force microscope (AFM) measurements,[23,38,39] and simulations.[44] Closer examination of the variations in shell thickness determined at varying particle concentrations and shear rates, and comparison of dynamic and static measurements, suggests that a more detailed analysis can provide further information about the nanostructure of this solvation layer. The molecular structure for confined layers of related ionic liquids have been proposed based on surface forces measurements and molecular packing parameters.[43] Such an analysis will require a full theory for the dispersion forces and electrostatic forces acting between highly curved surfaces, such as those of the nanoparticles, with such nanostructured solvation layers, which goes well beyond the scope of this work. The comprehensive data presented here, collected using a variety of measurement techniques, not only provides a database with which such theories can be rigorously tested, but also acts as guidance for the development of future theories.

Molecular design of a surface coating to induce specific molecular interactions between the particle surface and the ionic liquid with the intent to local specific solvent structuring is demonstrated as a method to create spontaneous dispersion and stabilization of nanoparticles that are otherwise not dispersible in ionic liquids. The resultant solvation layers impart colloidal stability, but also lead to larger effective volume fractions in solution. The presence of ubiquitous dispersion forces and the solvation layer will ultimately limit the total concentration of particles dispersible in the ionic liquids; however, we have successfully dispersed these particles up to 61 wt % corresponding to 45 vol %, which is a significant improvement on the current published maximum of

TABLE 6. Densities of Particles, Fluorocarbon and Solvents at 25 °C

	silica	coated silica	fluorocarbon	$[C_4mim][BF_4]$	H_2O	ethanol
ρ (g/cm^3)	2.210 ± 0.005	2.167 ± 0.007	1.646[a]	1.201 ± 0.001	0.997 ± 0.001	0.789[a]

[a] The densities of fluorocarbon and ethanol are from material safety data sheet. All the others are measured or calculated from densitometry.

20 wt % particle content. Important questions remain as to the thermal stability and particle size dependence of these solvation layers that will be addressed in future work.

METHODS

Particle Coating. Colloidal silica dioxide nanoparticles (NexSil 125−40, nominal radius 42.5 nm) were purchased from Nyacol Nano Technologies, Inc. and used as received (40 wt % solid in H_2O with sodium stabilizing counterion as supplied). Scanning electron microscopy (SEM) analysis shows an average radius of ~45 nm (Supporting Information) in agreement with the manufacturer, which is smaller than the size obtained from DLS due to polydispersity. 9-Carbon chain fluorocarbon 1*H*,1*H*,9*H*-hexadecafluoro-1-nonanol (CAS 376−18−1, $C_9H_4F_{16}O$) was selected for surface modification of the silica particles (Figure 2A). The fluorocarbon (from Matrix Scientific) was covalently grafted to the nanoparticle surface *via* an dehydration reaction following the protocol of van Helden *et al.*[53] After the reaction, the modified nanoparticles were thoroughly washed 3 times with ethanol using a Sorvall RC6+ centrifuge. Finally, the particles were stored in ethanol until use, and no visual sedimentation was observed, even after 4 months. The chemical grafting was confirmed by proton nuclear magnetic resonance (^{1}H NMR) using a Bruker AV-400 instrument (see Supporting Information). The grafting density of the fluorocarbon was determined to be 1.4 chains/nm^2 and the particle surface coverage was 60% as determined by thermogravimetric analysis (TGA, TA Instruments Q500) measurement (see Supporting Information).

Sample Preparation. The ionic liquid $[C_4mim][BF_4]$ (99% pure, Iolitec, Figure 2B), was dehydrated under vacuum condition at 70 °C for 24 h prior to use. The final water content was 373 ppm as determined by the Karl Fischer titration.

Dispersions of coated particles were prepared by first drying the fluorocarbon-coated silica under a nitrogen stream and then under vacuum for 24 h. The particles were dispersed in dehydrated ionic liquid at varying concentrations from dilute through concentrated. For the uncoated silica particle dispersions, the particles were thoroughly washed 3 times with water using a Sorvall RC6+ centrifuge to remove the sodium stabilizer before sample preparation. All the dispersions were mixed using a vortex mixer (3 min at 3000 rpm), sonication water bath (4 h at room temperature) and roll mixer (72 h at room temperature) to ensure homogeneity, followed by a 5 min degassing to remove air bubbles in the samples. As the presence of water decreases the structure of solvation layer and reduce the particle stability,[26,45] the samples were dehydrated again in a vacuum oven at 70 °C for 24 h prior to each measurement and the water content was 1194 ppm as measured by the Karl Fischer titration. All of the dispersion samples were prepared by weight and converted to volume fraction using the measured particle and solvent densities (Table 6). The coated particles in $[C_4mim][BF_4]$ dispersion samples are stable at room temperature and no sedimentation is observed after 6 months.

Transmission Electron Microscopy (TEM). Images of the nanoparticles were recorded using a JEOL JEM-2000FX (LaB6) TEM operated at 200 kV in the Keck Microscope facility at the University of Delaware. The dried, coated particles were imaged after the ethanol of coated particle/ethanol solution drops dried on the carbon-sputtered copper grid. The coated particles dispersed in $[C_4mim][BF_4]$ were imaged directly in their solution phase. Samples were prepared by placing a small droplet of dilute coated particle/$[C_4mim][BF_4]$ dispersion onto a carbon-sputtered copper grid and extra solution was removed by blotting with filter paper, leaving a thin film of dispersion on the grid.

Densitometry. The solvent and dispersion densities were measured using an Anton Paar DMA-4500 M densitometer. Particle density in solution was calculated from a dilution series of six concentrations with particle mass fraction $0 \le x < 0.02$. For the uncoated silica, the stock NexSil solution ($x = 0.415 \pm 0.006$) was diluted with a solution of 0.1 mM NaCl nanopure H_2O solution (pH = 9.1 ± 0.1) to maintain particle stability and match the mother liquid. The fluorocarbon-coated silica was dispersed into $[C_4mim][BF_4]$, a good solvent for the fluorocarbon brush. Assuming ideal mixing of the dispersion constituents, the particle density can be extracted using the following equation based on ideal mixing:

$$\frac{1}{\rho_{solution}} = \left(\frac{1}{\rho_{particles}} - \frac{1}{\rho_{solvent}}\right)x + \frac{1}{\rho_{solvent}} \quad (1)$$

where, $\rho_{solution}$, $\rho_{particles}$, and $\rho_{solvent}$ are the solution density, particle density, and solvent density, respectively; x is the mass fraction of particles in solution. Data are presented in the Supporting Information.

Dynamic Light Scattering (DLS). The intensity autocorrelation function of dilute dispersions was measured using a Brookhaven Instruments ZetaPals dynamic light scattering (DLS) at 25 °C. The instrument optimized the incident laser power at start of each measurement with incident photon wavelength $\lambda = 658$ nm and the scattered light intensity was detected by a photodetector at a scattering angle $\theta = 90°$. The magnitude of the momentum transfer vector, $q = 4\pi n_0/\lambda \sin(\theta/2)$, is fixed, where n_0 is the refractive index of the sample. For this system $q = 0.025$ nm^{-1}, for $n_0 \sim 1.4$ ($[C_4mim][BF_4]$, $n_0 = 1.42$, and silica dioxide, $n_0 = 1.46$). The autocorrelation function was measured over a period of 120 s and the average decay time was extracted by fitting to a second-order cumulant expansion through ZetaPals software. The average decay rate Γ is related to the diffusion coefficient D by

$$\Gamma = q^2 D \quad (2)$$

The hydrodynamic radius R_H of the particles is then calculated from the Stokes−Einstein relation

$$D = \frac{k_B T}{6\pi\mu R_H} \quad (3)$$

where μ is viscosity of solvent ($[C_4mim][BF_4]$, $\mu = 106.5$ cP), k_B is Boltzmann's constant, which is 1.38×10^{-23} J/K, and T is the absolute temperature.

Derjaguin−Landau−Verwey−Overbeek (DLVO) Calculation. According to the DLVO theory, the total interparticle potential $\Phi_{total}(d)$ can be written as the sum of an attractive London-van der Waals potential $\Phi_{vdw}(d)$ and a repulsive electrostatic potential $\Phi_{vdw}(d)$ due to the charge of the particles.[32]

$$\Phi_{total}(d) = \Phi_{vdw}(d) + \Phi_{ele}(d) \quad (4)$$

where d is the distance between the particle surfaces. $\Phi_{vdw}(d)$ between two identical spherical silica particles of radius r is given by[54]

$$\Phi_{vdw} = -\frac{1}{6}A\left(\frac{2r^2}{a^2-4r^2}+\frac{2r^2}{a^2}+\ln\frac{a^2-4r^2}{a^2}\right) \quad (5)$$

where a is the two particles center−center separation, $a = 2r + d$. A is the Hamaker constant (two silica dioxide phases interacting across solvent) and can be calculated from the relative dielectric constant ε and refractive index n of silica dioxide and solvent based on the Lifshitz theory

$$A = \frac{3}{4}k_BT\left(\frac{\varepsilon_p-\varepsilon_s}{\varepsilon_p+\varepsilon_s}\right)^2+\frac{3h\nu_e}{16\sqrt{2}}\frac{(n_p^2-n_s^2)^2}{(n_p^2+n_s^2)^{3/2}} \quad (6)$$

where k_B is the Bolzmann constant, T is the absolute temperature, h is Planck's constant, which is 6.63×10^{-34} J·s, and ν_e is the frequency of the main electronic absorption for the dielectric permittivity, which can be taken to be 3×10^{15} s^{-1} for water and [C_4mim][BF_4]. The Hamaker constant of silica particles in mother liquid is assumed to be identical as for that in H_2O.

The repulsive electrostatic potential Φ_{vdw} (d) of spheres with thin double-layers in ionic liquids and with constant potential in H_2O are given respectively by[55]

$$\Phi_{ele} = 32\pi r\varepsilon_s\varepsilon_0\left(\frac{k_BT}{ze}\right)^2\tanh^2\left(\frac{\psi_s ez}{4k_BT}\right)\exp(-\kappa d) \quad (7)$$

$$\Phi_{ele} = 2\pi r\varepsilon_s\varepsilon_0\left(\frac{k_BT}{ze}\right)^2\left(\frac{\psi_s ez}{k_BT}\right)^2\ln(1+e^{-\kappa d}) \quad (8)$$

where ε_s is the relative dielectric permittivity of solvent, ε_0 is dielectric constant, which is 8.85×10^{-12} $C^2/(J\cdot m)$, z is the symmetric electrolyte of valence, e is unit charge 1.60×10^{-19} C, ψ_s is the surface potential, and κ is the Debye reciprocal length parameter. Debye length κ^{-1} is calculated as follows[54]

$$\kappa^{-1} = \sqrt{\frac{\varepsilon_s\varepsilon_0k_BT}{1000e^2N_A(\sum_i z_i^2M_i)}} \quad (9)$$

where z_i is the electrolyte valence of solvent, M_i is the molar concentration of electrolyte, and N_A is the Avogadro's number, which is 6.02×10^{-23} mol^{-1}.

The zeta potential is used as an estimation of nanoparticle surface potential for the electrostatic force calculation. Because of the high ionic strength and nonaqueous feature of ionic liquid [C_4mim][BF_4], it was difficult to measure the zeta potential with a conventional electrokinetic method in the ionic liquid colloid system.[27] The zeta potential of silica particles in [C_4mim][BF_4] is calculated by assuming the charge density of silica nanoparticles in [C_4mim][BF_4] is the same as that measured in the sodium chloride (NaCl) aqueous solution of 1.25 M concentration. The Debye length in ionic liquid [C_4mim][BF_4] is estimated from electrical double layer measurement using sum frequency generation vibrational spectroscopy (SFG), electrochemical impedance spectroscopy (EIS).[34] Uncoated silica particles are dispersed in aqueous solution (0.1 mM (pH = 9.1 ± 0.1) NaCl solution: mother liquid) to measure the zeta potential of silica nanoparticles in the aqueous solution using a Brookhaven ZetaPals instrument.

Small Angle Neutron Scattering (SANS). SANS measurements were performed at the National Institute of Standards and Technology (NIST) Center for Neutron Research (NCNR) in Gaithersburg, MD on both NG3 and NG7 beamlines. Samples were loaded into demountable titanium cells with a 1 mm path length. The cell temperatures were maintained to ±0.1 °C using the 10 CB, 10 position sample cell holder with fluid bath. A wide range in scattering wavevector q was obtained by combining scattering intensity from four different instrument configurations at detector distances of 1, 4, 13, and 15.3 m with lens. The wavelength for 1, 4, and 13 m configurations is 6.0 and 8.0 Å for 15.3 m with lens. The SANS scattering intensity profiles were reduced to absolute scale and analyzed with the NIST data reduction and analysis macros in IGOR Pro available from NIST.[47] The total background was calculated from the slope of the Porod plot (Iq^4 *versus* q^4), and subtracted from all SANS spectra.

SANS Data Analysis. The scattering length density (SLD) of particles and solvents were calculated using measured densities (Table 6) by NIST NCNR online tools: Neutron activation and scattering calculator.[56] Properties of the dispersions were determined by modeling the measured SANS intensity using a form factor model for polydisperse core−shell particles (core−shell with Schultz distributed core) and a monodisperse structure factor model that includes hard core repulsion with contact attraction (sticky hard sphere model). The SANS spectra of particle solutions are described by the function

$$I(q) = n_p\bar{P}(q, \rho_{i(SLD)}, \phi, \bar{r}, p, \delta)S(q, \phi_{eff}, \bar{r}_{eff}, \tau, \varepsilon) + bkg \quad (10)$$

where n_p is the particle number density, $n_p = \phi/\langle V\rangle$, $\langle V\rangle$ is the average of single particle volume, and bkg is the background level. $\bar{P}(q,\rho_i,\phi,,p,\delta)$ is the form factor, which describes the scattering from individual particles, and is a function of wavevector q, particle, solvent, and shell scattering length density $\rho_{i(SLD)}$, particle volume fraction ϕ, core particle average size , polydispersity p, and shell thickness δ. $S(q,\phi_{eff,eff},\tau,\varepsilon)$ is the structure factor, which contains information on interparticle interactions and spatial arrangement of particles, and it is a function of wavevector q, effective particle volume fraction ϕ_{eff}, effective particle average size $_{eff}$, interaction parameter τ (Baxter temperature) and ε (perturbation parameter). The structure factor is calculated using the Ornstein−Zernike[57] (OZ) equation with the Percus−Yevick[58] (PY) closure approximation scaled by the mean effective particle diameter. For dilute dispersions, the interactions between particles can be ignored and the structure factor $S(q,\phi_{eff,eff},\tau,\varepsilon) \sim 1$.

The expression for the core−shell form factor with Schultz distributed core and constant shell is

$$\bar{P}(q, \rho_i, \phi, \bar{r}, p, \delta) = \int_0^\infty f(R, \bar{r}, p)[(\rho_{shell}-\rho_{solvent})F(q, R+\delta) + (\rho_{core}-\rho_{shell})F(q, R)]^2\, dR \quad (11)$$

where $f(R)$ is the Schultz distribution function. The interference factor $F(q, R)$ is that for a spherical object in the Rayleigh−Gans−Debye limit.[59]

$$F(q, R) = 3V_p\frac{\sin(qR)-qR\cos(qR)}{(qR)^3} \quad (12)$$

Rheology. Rheological measurements were performed on a TA Instruments AR-G2 stress controlled rheometer at 25 °C with Peltier plate temperature control, and a 40 mm stainless steel cone with 2° cone angle with solvent trap. Conversion between applied and measured parameters (torque M and strain γ) and the rheological material functions were performed using the TA Instruments Trios software. To erase any previous shear histories and maintain a consistency between measurements, a steady preshear was applied at a shear stress of 10 Pa for 2 min before each dynamic rheological measurement. Each measurement was repeated three times for accuracy.

Conflict of Interest: The authors declare no competing financial interest.

Acknowledgment. The financial support for this work was partially provided by the National Aeronautics and Space Administration EPSCoR Grant (No: NNX11AQ28A). We acknowledge the support of the National Institute of Standards and Technology, U.S. Department of Commerce, in providing the neutron research facilities used in this work. This work utilized facilities supported in part by the National Science Foundation under Agreement No. DMR-0944772. The statements, findings, conclusions and recommendations are those of the authors and do not necessarily reflect the view of NIST or the U.S. Department of Commerce. We acknowledge the W. M. Keck Electron Microscopy Facility at the University of Delaware for use of their TEM and SEM instruments. We thank Prof. Chaoning Ni for his help with *in situ* TEM image. We thank Wei-Fan Kuan for help with NMR measurement. We also thank Prof. Michael Mackay and Roddel Remy for assistance with TGA.

Supporting Information Available: Thermogravimetric analysis (TGA), dynamic light scattering (DLS) measurement, silica particle density analyses, NMR measurements, and SEM. This material is available free of charge *via* the Internet at http://pubs.acs.org.

REFERENCES AND NOTES

1. Welton, T. Room-Temperature Ionic Liquids. Solvents for Synthesis and Catalysis. *Chem. Rev.* **1999**, *99*, 2071–2084.
2. Dupont, J.; de Souza, R. F.; Suarez, P. A. Ionic Liquid (Molten Salt) Phase Organometallic Catalysis. *Chem. Rev.* **2002**, *102*, 3667–3692.
3. Sheldon, R. Catalytic Reactions in Ionic Liquids. *Chem. Commun.* **2001**, 2399–2407.
4. Wasserscheid, P.; Keim, W. Ionic Liquids—New "Solutions" For Transition Metal Catalysis. *Angew. Chem., Int. Ed.* **2000**, *39*, 3772–3789.
5. Lee, S.-Y.; Ogawa, A.; Kanno, M.; Nakamoto, H.; Yasuda, T.; Watanabe, M. Nonhumidified Intermediate Temperature Fuel Cells Using Protic Ionic Liquids. *J. Am. Chem. Soc.* **2010**, *132*, 9764–9773.
6. Zakeeruddin, S. M.; Graetzel, M. Solvent-Free Ionic Liquid Electrolytes for Mesoscopic Dye-Sensitized Solar Cells. *Adv. Funct. Mater.* **2009**, *19*, 2187–2202.
7. Crosthwaite, J. M.; Muldoon, M. J.; Dixon, J. K.; Anderson, J. L.; Brennecke, J. F. Phase Transition and Decomposition Temperatures, Heat Capacities and Viscosities of Pyridinium Ionic Liquids. *J. Chem. Thermodyn.* **2005**, *37*, 559–568.
8. Valkenburg, M. E. V.; Vaughn, R. L.; Williams, M.; Wilkes, J. S. Thermochemistry of Ionic Liquid Heat-Transfer Fluids. *Thermochim. Acta* **2005**, *425*, 181–188.
9. Hough, W. L.; Smiglak, M.; Rodriguez, H.; Swatloski, R. P.; Spear, S. K.; Daly, D. T.; Pernak, J.; Grisel, J. E.; Carliss, R. D.; Soutullo, M. D.; *et al.* the Third Evolution of Ionic Liquids: Active Pharmaceutical Ingredients. *New J. Chem.* **2007**, *31*, 1429–1436.
10. Street, K. W.; Morales, W.; Koch, V. R.; Valco, D. J.; Richard, R. M.; Hanks, N. Evaluation of Vapor Pressure and Ultra-High Vacuum Tribological Properties of Ionic Liquids. *Tribol. Trans.* **2011**, *54*, 911–919.
11. Morales, W.; Street, K. W.; Richard, R. M.; Valco, D. J. Tribological Testing and Thermal Analysis of an Alkyl Sulfate Series of Ionic Liquids for Use as Aerospace Lubricants. *Tribol. Trans.* **2012**, *55*, 815–821.
12. Liu, W. M.; Ye, C. F.; Gong, Q. Y.; Wang, H. Z.; Wang, P. Tribological performance of room-temperature ionic liquids as lubricant. *Tribol. Lett.* **2002**, *13*, 81–85.
13. Seo, S.; Quiroz-Guzman, M.; DeSilva, M. A.; Lee, T. B.; Huang, Y.; Goodrich, B. F.; Schneider, W. F.; Brennecke, J. F. Chemically Tunable Ionic Liquids with Aprotic Heterocyclic Anion (AHA) for CO_2 Capture. *J. Phys. Chem. B* **2014**, *118*, 5740–5751.
14. Gomes, M. F. C.; Lopes, J. N. C.; Padua, A. A. H. Thermodynamics and Micro Heterogeneity of Ionic Liquids. *Ionic Liquids* **2009**, *290*, 161–183.
15. Antonietti, M.; Kuang, D.; Smarsly, B.; Zhou, Y. A. C. Ionic Liquids for the Convenient Synthesis of Functional Nanoparticles and Other Inorganic Nanostructures. *Angew. Chem., Int. Ed.* **2004**, *43*, 4988.
16. Scheeren, C. W.; Machado, G.; Dupont, J.; Fichtner, P. F.; Texeira, S. R. Nanoscale Pt (0) Particles Prepared in Imidazolium Room Temperature Ionic Liquids: Synthesis from an Organometallic Precursor, Characterization, And Catalytic Properties in Hydrogenation Reactions. *Inorg. Chem.* **2003**, *42*, 4738–4742.
17. Wei, G.-T.; Yang, Z.; Lee, C.-Y.; Yang, H.-Y.; Wang, C. R. C. Aqueous-Organic Phase Transfer of Gold Nanoparticles and Gold Nanorods Using an Ionic Liquid. *J. Am. Chem. Soc.* **2004**, *126*, 5036–5037.
18. Migowski, P.; Dupont, J. Catalytic Applications of Metal Nanoparticles in Imidazolium Ionic Liquids. *Chem.—Eur. J.* **2007**, *13*, 32–39.
19. Lopez-Barron, C. R.; Basavaraj, M. G.; DeRita, L.; Wagner, N. J. Sponge-to-Lamellar Transition in a Double-Tail Cationic Surfactant/Protic Ionic Liquid System: Structural and Rheological Analysis. *J. Phys. Chem. B* **2012**, *116*, 813–822.
20. Lopez-Barron, C. R.; Li, D. C.; DeRita, L.; Basavaraj, M. G.; Wagner, N. J. Spontaneous Thermoreversible Formation of Cationic Vesicles in a Protic Ionic Liquid. *J. Am. Chem. Soc.* **2012**, *134*, 20728–20732.
21. López-Barrón, C. R.; Li, D.; Wagner, N. J.; Caplan, J. L. Triblock Copolymer Self-Assembly in Ionic Liquids: Effect of PEO Block Length on the Self-Assembly of PEO—PPO—PEO in Ethylammonium Nitrate. *Macromolecules* **2014**, *47*, 7484–7495.
22. Bai, Z.; Lodge, T. P. Polymersomes with Ionic Liquid Interiors Dispersed in Water. *J. Am. Chem. Soc.* **2010**, *132*, 16265–16270.
23. Ueno, K.; Watanabe, M. from Colloidal Stability in Ionic Liquids to Advanced Soft Materials Using Unique Media. *Langmuir* **2011**, *27*, 9105–9115.
24. Ueno, K.; Imaizumi, S.; Hata, K.; Watanabe, M. Colloidal Interaction in Ionic Liquids: Effects of Ionic Structures and Surface Chemistry on Rheology of Silica Colloidal Dispersions. *Langmuir* **2009**, *25*, 825–831.
25. Smith, J.; Webber, G. B.; Warr, G. G.; Atkin, R. Silica Particle Stability and Settling in Protic Ionic Liquids. *Langmuir* **2014**, *30*, 1506–1513.
26. Smith, J. A.; Werzer, O.; Webber, G. B.; Warr, G. G.; Atkin, R. Surprising Particle Stability and Rapid Sedimentation Rates in an Ionic Liquid. *J. Phys. Chem. Lett.* **2009**, *1*, 64–68.
27. Ueno, K.; Inaba, A.; Kondoh, M.; Watanabe, M. Colloidal Stability of Bare and Polymer-Grafted Silica Nanoparticles in Ionic Liquids. *Langmuir* **2008**, *24*, 5253–5259.
28. Ueno, K.; Hata, K.; Katakabe, T.; Kondoh, M.; Watanabe, M. Nanocomposite Ion Gels Based on Silica Nanoparticles and an Ionic Liquid: Ionic Transport, Viscoelastic Properties, And Microstructure. *J. Phys. Chem. B* **2008**, *112*, 9013–9019.
29. Wittmar, A.; Gajda, M.; Gautam, D.; Dörfler, U.; Winterer, M.; Ulbricht, M. Influence of the Cation Alkyl Chain Length of Imidazolium-Based Room Temperature Ionic Liquids on the Dispersibility of TiO_2 Nanopowders. *J. Nanopart. Res.* **2013**, *15*, 1–12.
30. Wittmar, A.; Ruiz-Abad, D.; Ulbricht, M. Dispersions of Silica Nanoparticles in Ionic Liquids Investigated with Advanced Rheology. *J. Nanopart. Res.* **2012**, *14*, 1–10.
31. Mewis, J.; Wagner, N. J. *Colloidal Suspension Rheology*; Cambridge University Press: New York, 2012.
32. Israelachvili, J. N. *Intermolecular and Surface Forces*, 3rd ed.; Elsevier Academic Press, Inc.: San Diego, 2011; pp 1—674.
33. Lanning, O. J.; Madden, P. A. Screening at a Charged Surface by a Molten Salt. *J. Phys. Chem. B* **2004**, *108*, 11069–11072.
34. Baldelli, S. Probing Electric Fields at the Ionic Liquid—Electrode Interface Using Sum Frequency Generation Spectroscopy and Electrochemistry. *J. Phys. Chem. B* **2005**, *109*, 13049–13051.
35. Lynden-Bell, R. M.; Del Pópolo, M. G.; Youngs, T. G. A.; Kohanoff, J.; Hanke, C. G.; Harper, J. B.; Pinilla, C. C. Simulations of Ionic Liquids, Solutions, and Surfaces. *Acc. Chem. Res.* **2007**, *40*, 1138–1145.
36. Feng, G.; Qiao, R.; Huang, J.; Dai, S.; Sumpter, B. G.; Meunier, V. The Importance of Ion Size and Electrode Curvature on Electrical Double Layers in Ionic Liquids. *Phys. Chem. Chem. Phys.* **2011**, *13*, 1152–1161.
37. Nordström, J.; Aguilera, L.; Matic, A. Effect of Lithium Salt on the Stability of Dispersions of Fumed Silica in the Ionic Liquid BMImBF4. *Langmuir* **2012**, *28*, 4080–4085.
38. Hayes, R.; Warr, G. G.; Atkin, R. At the Interface: Solvation and Designing Ionic Liquids. *Phys. Chem. Chem. Phys.* **2010**, *12*, 1709–1723.
39. Atkin, R.; Warr, G. G. Structure in Confined Room-Temperature Ionic Liquids. *J. Phys. Chem. C* **2007**, *111*, 5162–5168.
40. Ueno, K.; Kasuya, M.; Watanabe, M.; Mizukami, M.; Kurihara, K. Resonance Shear Measurement of Nanoconfined Ionic Liquids. *Phys. Chem. Chem. Phys.* **2010**, *12*, 4066–4071.

41. Segura, J. J.; Elbourne, A.; Wanless, E. J.; Warr, G. G.; Voïtchovsky, K.; Atkin, R. Adsorbed and near Surface Structure of Ionic Liquids at a Solid Interface. *Phys. Chem. Chem. Phys.* **2013**, *15*, 3320–3328.
42. Perkin, S.; Crowhurst, L.; Niedermeyer, H.; Welton, T.; Smith, A. M.; Gosvami, N. N. Self-Assembly in the Electrical Double Layer of Ionic Liquids. *Chem. Commun.* **2011**, *47*, 6572–6574.
43. Smith, A. M.; Lovelock, K. R. J.; Perkin, S. Monolayer and Bilayer Structures in Ionic Liquids and Their Mixtures Confined to Nano-Films. *Faraday Discuss.* **2013**, *167*, 279–292.
44. Pinilla, C.; Del Pópolo, M. G.; Lynden-Bell, R. M.; Kohanoff, J. Structure and Dynamics of a Confined Ionic Liquid. Topics of Relevance to Dye-Sensitized Solar Cells. *J. Phys. Chem. B* **2005**, *109*, 17922–17927.
45. Szilagyi, I.; Szabo, T.; Desert, A.; Trefalt, G.; Oncsik, T.; Borkovec, M. Particle Aggregation Mechanisms in Ionic Liquids. *Phys. Chem. Chem. Phys.* **2014**, *16*, 9515–9524.
46. Shiflett, M. B.; Yokozeki, A. Solubility of Fluorocarbons in Room Temperature Ionic Liquids. In *Ionic Liquids: From Knowledge to Application*; Plechkova, N. V., Rogers, R. D., Seddon, K. R., Eds.; American Chemical Society: Washington, D.C., 2009; Vol. 1030, pp 21−42.
47. Kline, S. R. Reduction and Analysis of SANS and USANS Data Using IGOR Pro. *J. Appl. Crystallogr.* **2006**, *39*, 895–900.
48. Van der Werff, J.; De Kruif, C. Hard-Sphere Colloidal Dispersions: The Scaling of Rheological Properties with Particle Size, Volume Fraction, And Shear Rate. *J. Rheol.* **1989**, *33*, 421–454.
49. Russel, W. B.; Wagner, N. J.; Mewis, J. Divergence in the Low Shear Viscosity for Brownian Hard-Sphere Dispersions: At Random Close Packing or the Glass Transition? *J. Rheol.* **2013**, *57*, 1555–1567.
50. Shenoy, S. S.; Wagner, N. J. Influence of Medium Viscosity and Adsorbed Polymer on the Reversible Shear Thickening Transition in Concentrated Colloidal Dispersions. *Rheol. Acta* **2005**, *44*, 360–371.
51. Lakshmi-narasimhan, K.; Wagner, N. J. The Influence of Weak Attractive Forces on the Microstructure and Rheology of Colloidal Dispersions. *J. Rheol.* **2005**, *49*, 475–499.
52. Perkin, S. Ionic Liquids in Confined Geometries. *Phys. Chem. Chem. Phys.* **2012**, *14*, 5052–5062.
53. Van Helden, A.; Jansen, J. W.; Vrij, A. Preparation and Characterization of Spherical Monodisperse Silica Dispersions in Nonaqueous Solvents. *J. Colloid Interface Sci.* **1981**, *81*, 354–368.
54. Hiemenz, P. C.; Rajagopalan, R. *Principles of Colloid and Surface Chemistry, Revised and Expanded*; CRC Press: Boca Raton, FL, 1997; Vol. 14.
55. Russel, W. B.; Saville, D. A.; Schowalter, W. R. *Colloidal Dispersions*; Cambridge University Press: Cambridge, 1992.
56. Neutron activation and scattering calculator. http://www.ncnr.nist.gov/resources/activation/ (accessed 12/03/2014).
57. Ornstein, L. S.; Zernike, F. Acculental Deviations of Density and Opalescence at the Critical Point of a Simple Substance. *Proc. K. Ned. Akad. Wet.* **1914**, *17*, 793–806.
58. Percus, J. K.; Yevick, G. J. Analysis of Classical Statistical Mechanics by Means of Collective Coordinates. *Phys. Rev.* **1958**, *110*, 1–13.
59. Glatter, O.; Kratky, O. *Small Angle X-ray Scattering*; Academic Press: Waltham, MA, 1982.